Population Study of Astrophysical False Positive Detections in the Southern PLATO field

Monthly Notices of the ROYAL ASTRONOMICAL SOCIETY

MNRAS **518,** 3637–3652 (2023) https://doi.org/10.1093/mnras/stac3262
Advance Access publication 2022 November 12

Population study of astrophysical false positive detections in the southern PLATO field

J. C. Bray,[1,2]★ U. Kolb,[1] P. Rowden,[3] Robert Farmer,[4] A. Börner[5] and O. Kozhura[1]

[1]*The Open University, School of Physical Sciences, Walton Hall, Milton Keynes MK7 6AA, UK*
[2]*Department of Physics, University of Auckland, Private Bag 92019, New Zealand*
[3]*Royal Astronomical Society, Burlington House, Piccadilly, London W1J 0BQ, UK*
[4]*Max-Planck-Institut für Astrophysik, Karl-Schwarzschild-Straße 1, D-85741 Garching, Germany*
[5]*German Aerospace Centre, Institute of Optical Sensor Systems, Rutherfordstr 2, D-12489 Berlin, Germany*

Accepted 2022 November 7. Received 2022 November 6; in original form 2022 May 8

ABSTRACT

For the upcoming PLAnetary Transits and Oscillation of stars (PLATO) satellite mission, a large number of target stars are required to yield a statistically significant number of planet transits. Locating the centres of the long duration observational phase (LOP) fields closer to the Galactic plane will increase the target star numbers but also the astrophysical false positives (FPs) from blended eclipsing binary systems. We utilize the Binary Stellar Evolution and Population Synthesis code, to create a complete synthetic stellar and planetary population for the proposed southern LOP field (LOPS0), as well as for a representative portion of the northern LOP field (LOPN-sub). For LOPS0, we find an overall low FP rate for planets smaller than Neptunes. The FP rate generally shows little variation with Galactic longitude (l), and a modest increase with decreasing Galactic latitude ($|b|$). The location of the LOPS field centre within the current allowed region is not strongly constrained by FPs. Analysis of LOPN-sub suggests a markedly increased number of FPs across the full range of planet radii at low $|b|$ resulting in approximately twice the percentage of FP detection rate in the LOPN-sub compared to the corresponding southern field segment in the planet radius range $-0.2 < \log(R/R_\oplus) \leq 0.4$. However, only a few per cent of fully eclipsing FPs in LOPS0 in this radius range have periods between 180 and 1000 d so the vast majority of FPs are expected to be outside the period range of interest for PLATO.

Key words: methods: numerical – eclipses – planets and satellites: detection – planets and satellites: terrestrial planets – binaries: eclipsing.

1 INTRODUCTION

The European Space Agency (ESA) satellite mission, PLAnetary Transits and Oscillation of stars (PLATO), is currently well into the construction phase with the satellite tentatively scheduled for launch in 2026. While other missions, such as *Kepler* (Batalha et al. 2010) and more recently the *Transiting Exoplanet Survey Satellite* (*TESS*; Ricker et al. 2014), have made a significant number of exoplanet discoveries, the PLATO mission is arguably unique in that it has the capability of detecting a large number of Earth-like planets orbiting Sun-type stars (Rauer et al. 2014). Like *TESS* and *Kepler* before it, PLATO aims to find exoplanets using the planetary transit method, where a reduction in flux from the target star is detected as a planet, or planets, transit across it. Such a detection requires that the planet and the star are aligned when viewed from the satellite. Due to the low probability of this occurring, especially for small planets at large orbital distances such as Earth-like planets around Sun-type stars, a large number of target stars need to be observed if a statistically significant sample of transiting exoplanets is to be detected. As an indication, the 2014 PLATO mission proposal set a target of >267 000 stars to be observed for the two long duration observational phases (LOPs; Rauer et al. 2014). The added constraints introduced by the resolution of the detectors, the noise to signal ratio required for a successful detection and the need for ground-based radial velocity follow-up measurements in particular, mean that the target stars need to be relatively bright, ideally within the priority magnitude range of $m_v < 16$.

The current proposal for the LOPs is to observe two fields of approximately 2,232 square degrees, one located in the Northern hemisphere (the LOPN), and the other in the Southern hemisphere (the LOPS), each for a duration of 2 yr; however, the final observing strategy is not expected to be finalized until 2 yr before the launch. The 2-yr minimum observation period is designed to fulfill one of PLATO's primary goals, which is to find Earth analogue planets (Rauer & Heras 2018).

With such a large field of view (FOV), and short focal length, a large pixel scale is required to cover the field. For PLATO this translates to an area of 15 by 15 arcsec (15 arcsec × 15 arcsec) per pixel. In addition, to reach the large number of target stars required, the observational fields must be located in regions with relatively high stellar densities. Logically, the denser the observational field the higher the likelihood of astrophysical false positives (FPs) from

★ E-mail: john.bray@open.ac.uk

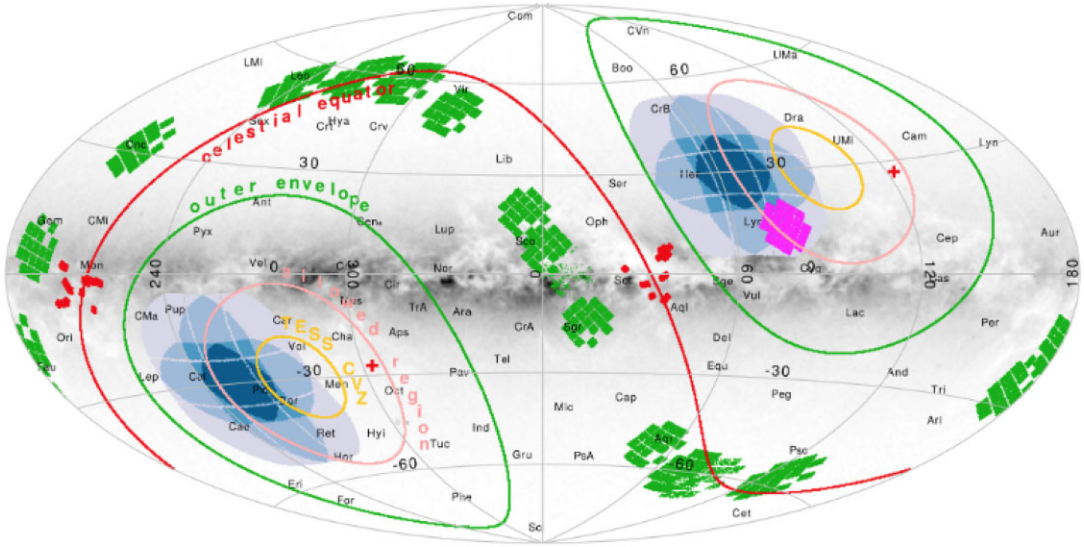

Figure 1. Aitoff projection in Galactic coordinates of the proposed Northern and Southern PLATO fields (blue), the area of the allowed PLATO field centres (shown as pink circles) and the total area covered by the allowed PLATO fields (shown as green circles). The CoRoT fields are shown as red squares, *Kepler* in magenta, K2 in green, and the *TESS* continuous viewing zones as yellow circles (Nascimbeni et al. 2022).

blended eclipsing binaries, since the foreground and background fields are also proportionately more dense.

In this work, we use the proposed southern PLATO LOP field (which we refer to as LOPS0), as a case study to quantify the dependency of both planetary transits (PTs) and astrophysical FPs, on Galactic longitude (l), and latitude (b). Using these dependencies and the clearly stated required minimum number of target stars, we seek to identify the optimal l and b pointing to minimize the percentage of FP detections (per centFP) which we define as the number of FPs divided by the number of FPs plus the number of PTs, expressed as a percentage.

This paper is set out as follows: In Section 2, we present a brief description of the PLATO mission relevant to our research. In Section 3, we describe the stellar evolution and population synthesis tools used to assess the expected PT and FP occurrences. We also examine the planetary and stellar distributions derived from the *Kepler* field and how these distributions can be used to calibrate our synthetic LOPS0. In Section 4, we outline our method of evaluating PTs and FPs for LOPS0 and present our results for this field. In Section 5, we fit functions to the PTs and FPs by l and b to evaluate how the location of the field centre affects these results. In Section 6, we use the functions derived in Section 5 to model the per centFP for different l and b field centre locations within the allowed region. In Section 7, we compare representative sub-fields of LOPS and LOPN, and finally in Section 8, we discuss our findings and present our conclusions.

2 THE PLATO MISSION

Below we outline the details of the PLATO mission relevant to our research. For a more comprehensive account of the mission and its aims refer to Rauer et al. (2014), Rauer & Heras (2018), and references therein. While we recognize that other phenomenon, such as stellar activity, can also result in FP planetary transit signals (Heller, Harre & Samadi 2022), in this research we focus only on FPs resulting from eclipsing binaries blended in the same pixels as the target stars.

2.1 Observing strategy

The PLATO mission is a 4-yr mission comprising two LOPs, one in the Southern hemisphere and one in the Northern hemisphere. Each of the LOPs will have a 2-yr duration. If the mission is extended, it is envisaged that a number of 'step-and-stare' phases will be added, covering additional areas of sky but for much shorter time intervals, most likely 2–5 months each.

The proposed LOP fields are 2232 square degrees with both constrained to have their centres located within spherical caps with the ecliptic coordinate $|\beta| > 63^\circ$. While the final field location will not be confirmed until two years before launch, the working assumption within the consortium is that the LOP field centres will not be significantly different from the two originally proposed LOP field centre locations, the Northern hemisphere LOP (LOPN), centred on Galactic coordinates $l = 65^\circ$ and $b = 30^\circ$ and the Southern hemisphere LOP (LOPS), centred on $l = 253^\circ$ and $b = -30^\circ$. Fig. 1 shows the locations of the proposed LOPN and LOPS fields along with the allowed regions for the LOPN and LOPS field centres and the maximum outer bounds. For context the corresponding footprints of the CoRoT, *Kepler*, and K2 surveys, as well as the *TESS* continuous viewing zones, are also shown.

2.2 PLATO target stars

The PLATO consortium has created the PLATO input catalogue (PIC) using data predominantly from *Gaia* DR2 (RD05) (Montalto et al. 2021). PIC1.1.0 includes PICtarget110, which identifies target stars in both the LOPN and the LOPS. It is envisaged that updated versions of the PIC will be released as more data are released from the *Gaia* mission and incorporated into the PIC.

The largest target group P5, is defined as stars with magnitude $m_v \leq 13.0$ of type F5 to late K with a maximum temperature of 6775 K and a minimum temperature of 3875 K (ESA-SCI 2017). For this research, we concentrate on the P5 target star group and predominantly on the proposed LOPS which we refer to as LOPS0. This location and target group have been selected as they provide the

largest number of stars and hence will produce the most statistically significant results.

Our analysis focuses on the possible blending of the target stars with background (or foreground), eclipsing binary systems. We consider only non-grazing eclipses of binary systems which, when blended with flux from the target star mask area, will produce a light-curve shape and flux variation similar in magnitude to a planetary transit.

3 STELLAR EVOLUTION AND POPULATION SYNTHESIS; TOOLS AND CALIBRATION

To determine the per centFP in LOPS0, we utilize the Binary Stellar Evolution and Population Synthesis (BISEPS), stellar models to create synthetic single and binary stellar populations for LOPS0 in its entirety.

To approximate the target star mask area of Marchiori et al. (2019), we subdivide LOPS0 into squares of 30 arcsec × 30 arcsec or four PLATO pixels. We then identify each four-pixel area where a target star could be found, i.e. each four-pixel square where the $m_v \leq 16$. We refer to these as PLATO 'superpixels' and assign each single star in these superpixels a single planet with a random orbital inclination angle. Where our simulations show that the angle of inclination for any system results in a planet transiting its host star, the flux reduction is calculated. If the flux reduction exceeds the total instrument noise, as calculated in Section 4.2, we class it as a detectable transit event and the corresponding apparent planet radius and orbital period is recorded taking into account blending from the background flux in the superpixel. Similarly, every binary system in our superpixel is assigned a random orbital inclination angle and a similar analysis is carried out for all non-grazing stellar eclipses.

3.1 Stellar evolution – The BISEPS code

BISEPS is a population synthesis tool developed by Willems & Kolb (2002). It uses large libraries of different metallicity single and binary stellar models to create Galactic populations. The stellar models are created using simplified binary evolution algorithms based on the prescriptions of Hurley, Pols & Tout (2000) and Hurley, Tout & Pols (2002). The algorithms consider mass-loss from stellar winds, angular momentum loss via gravitational waves, magnetic braking and Roche-lobe overflow. The code has been utilized in a number of stellar population studies (Willems & Kolb 2004; Willems, Kolb & Justham 2006; Davis, Kolb & Willems 2010; Farmer, Kolb & Norton 2013). Readers wanting more detail on the code should refer to the above studies.

The initial mass parameter space for the primary stars (M_1), is divided into 50 evenly spaced logarithmic bins between 0.1 and 20 $M_\odot$ and into 300 evenly spaced logarithmic orbital separation bins between 3 and 10^6 $R_\odot$. The secondary stars (M_2), are chosen from the same parameter space as M_1 but only systems where $M_1 > M_2$ are evolved. Initial orbits are assumed to be circular and subsequent orbits are kept circularized at each time-step. The equivalent circular period can be substituted because, as shown by Hurley et al. (2002), orbits generally circularize prior to Roche-lobe overflow so in binaries with the same semilatus rectum the outcome of the interactions is virtually independent of eccentricity.

For practical reasons, single stars are modelled as binary systems with an orbital period of 10^7 $R_\odot$. The primary mass parameter space (M_1) is divided into 10 000 evenly spaced logarithmic bins between 0.1 and 20 $M_\odot$ with the secondary star mass (M_2), set at 0.1 $M_\odot$.

3.2 Population synthesis

Population synthesis in BISEPS is carried out by randomly selecting single and binary models from the libraries created above. We assume a binary fraction of 0.5 and assign probabilities for each model using the primary star mass (M_1), and an initial mass function (IMF) following Kroupa, Tout & Gilmore (1993) with $\mathrm{d}N/\mathrm{d}M \propto M^\Gamma$ as follows:

$$\Gamma = \begin{cases} -1.3 \text{ for } M_1 < 0.5\,M_\odot \\ -2.2 \text{ for } 0.5 \leqslant M_1 < 1.0\,M_\odot \\ -2.7 \text{ for } 1.0\,M_\odot \leqslant M_1. \end{cases}$$

A Galactic structure is created assuming a thin disc with a metallicity of $Z = 0.02$ (Haywood 2001), embedded in a thick disc with a metallicity of $Z = 0.0033$ (Gilmore, Wyse & Jones 1995). The stellar density of both discs is modelled assuming the double exponential distribution outlined below:

$$\Omega(R_g, z) = \frac{1}{4\pi h_r^2 h_z} \exp\left(\frac{-R_g}{h_R}\right) \exp\left(\frac{-|z|}{h_z}\right) \quad (1)$$

with $h_R = 2.8$ kpc and $h_z = 300$ pc for the inner disc and $h_R = 3.7$ kpc and $h_z = 1$ kpc for the outer disc. The Sun is located at $R_g = 8.5$ kpc (Reid 1993) and and $z = 30$ pc (Chen et al. 2001). Star formation is assumed to occur in the thick disc for the first 3Gyr and in the thin disc from 3 to 15 Gyr. Our population includes single and binary stars down to a visual magnitude $m_v = 26$.

3.3 Stellar population and eclipsing binary calibration

We used the calibrated BISEPS models created by Farmer et al. (2013) for their study of the Kepler field. Applying the methods of the Kepler Stellar Classification program (Brown et al. 2011) to their synthetic Kepler field, Farmer et al. (2013) demonstrated a satisfactory match in $\log(g)$ versus $\log(T_{\rm eff})$ space with the real Kepler input catalogue (KIC; Koch et al. 2010). They then subjected the synthetic KIC to the Kepler target selection process to generate a synthetic Kepler target list. It is on the basis of this synthetic target list that we calibrate the eclipsing binary population of our synthetic population model.

For periods larger than about 10 d, the synthetic orbital period distribution of eclipsing binaries detectable by Kepler increases with decreasing period and satisfactorily matches the distribution of Kepler Eclipsing Binary Catalog KEBC; (Prša et al. 2011; Slawson et al. 2011; Conroy et al. 2014a,b; LaCourse et al. 2015; Abdul-Masih et al. 2016; Kirk et al. 2016). Below this value the KEBC period distribution flattens off while the synthetic distribution continues to rise, resulting in a model overprediction by about a factor of 2 for the number of these short-period binaries. The discrepancy is somewhat more pronounced when only those KEBC binaries with a morphology parameter (Matijevig et al. 2012), less than 0.7 are used, which restricts the sample to systems that are likely detached or semidetached, i.e. systems which cannot easily be identified as FPs in planet transit searches when blended with other stars. The orbital period discrepancy is related to an underrepresentation of unequal mass ratio (q) short-period binaries relative to the model.

We remove the discrepancy by introducing a calibration weighting for short-period systems in the synthetic sample ($P < 10$ d) which is proportional to $q^{2.5} \times f(\log P)$, where $f(\log P)$ increases effectively linearly from 0.4 at $P = 1$ d, to 1 at $P = 10$ d (see Rowden 2018 for more details).

Since our analysis was carried out some entries in the KEBC have been updated so we re-visited the KEBC to ascertain if our modified

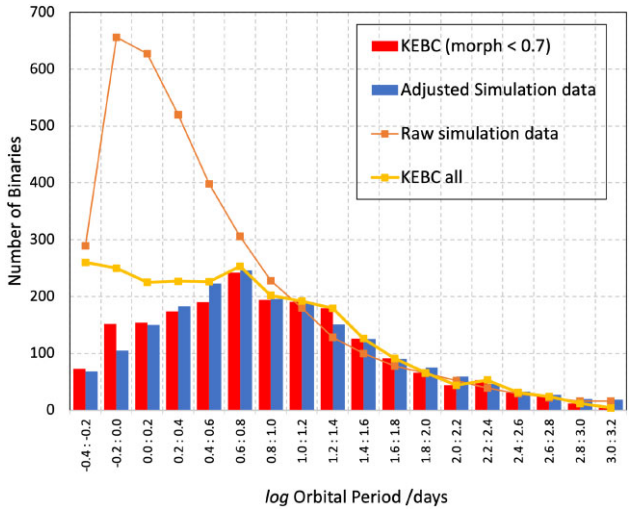

Figure 2. Observed versus simulated Kepler eclipsing binary distributions. The yellow line shows all *Kepler* eclipsing binaries, the orange line shows the raw simulation data, the red bars show the KEBC binary distribution with morphology parameter <0.7 and the blue bars shown the adjusted BiSEPS population synthesis binary distribution.

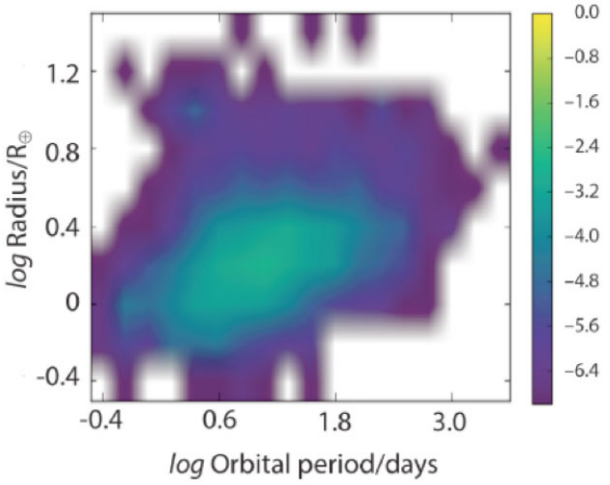

Figure 3. Observed *Kepler* exoplanet distribution. The contour scale is normalized and displayed in log space.

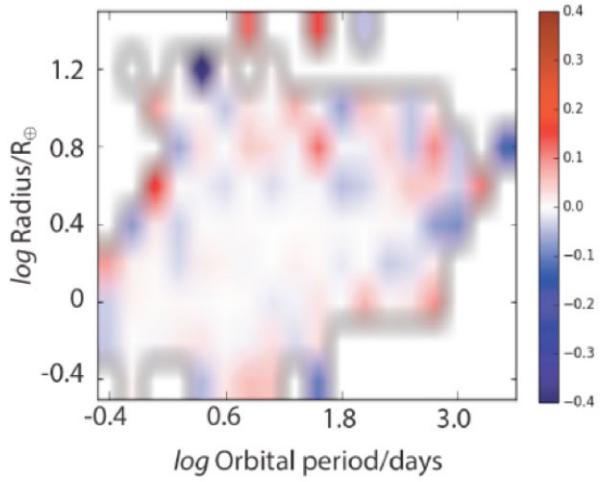

Figure 4. Relative difference between the observed Kepler exoplanet distribution and the detectable synthetic distribution. The contour scale represents the relative difference displayed in log space.

period distribution still provides a good approximation to the KEBC. We reanalysed the data in the KEBC Third Revision (last updated 2019 August 8). Fig. 2 shows the updated results for the entire KEBC (yellow line) and those with a morphology parameter <0.7 (red bars). We have reproduced, on the same plot, our original eclipsing binary period distribution (orange line) as well as the adjusted data set we described above (blue bars).

We find our original adjusted eclipsing binary period distribution is still a good approximation for the KEBC, especially the KEBC data with a morphology parameter of <0.7.

3.4 The intrinsic exoplanet distribution

We conducted a similar calibration exercise for the intrinsic planet content of the BiSEPS synthetic population model. In the synthetic Kepler field, we seeded each single star with one exoplanet, randomly chosen from an initially flat distribution in planet period (P) and planet radius (R). Each system was assigned a random orbital inclination angle. We then extracted those systems that displayed detectable transits according to the *Kepler* detector characteristics. We considered both the single 'long cadence' and 'benchmark' estimate sensitivities of the *Kepler* detectors as outlined in the *Kepler* instrument manual (Van Cleve & Caldwel 2016). The extracted detectable synthetic exoplanet distribution over P and R obtained above was then compared against the observed exoplanet distribution shown in Fig. 3 taken from the NASA Exoplanet Science Institute (NExScI)[1] catalogue of confirmed Kepler planets. We highlight that the relative distribution is over the planet radius of confirmed planets only. The combined group of confirmed and candidate planets is broadly similar for $\log R/R_\oplus > 0$, suggesting that completeness may be similar for both samples. The *Kepler* planet sample is least complete at long periods and small radii, making estimates in this parameter space particularly vulnerable to systematic uncertainties. Our model results for $\log R/R_\oplus < 0$ should be seen in this context.

[1] https://exoplanetarchive.ipac.caltech.edu/docs/data.html

The seeding probabilities were then iteratively adjusted for each P and R bin until a satisfactory match between the synthetic and observed exoplanet P and R distributions were achieved. After applying our selected adjustment matrix, we find the relative difference between the observed confirmed exoplanets and those produced by our synthetic population to be no more than 0.10 dex in the period / radius range of interest to the PLATO mission, namely planet period $\log P > 0$ and planet radii $0.0 < \log(R/R_\oplus) \leq 0.4$. The comparison is shown in Fig. 4.

With the seeding assumption of one planet per star this procedure leads to a synthetic planet sample which underestimates the total planet count in the Kepler field. While data from microlensing surveys suggests that there is at least one planet per star (Cassan et al. 2012), more recent studies of planets in the range $0.0 < \log(R/R_\oplus) \leq 1.0$ around M dwarfs suggest this number is more likely to be between 1.3 and 2.5 (Feliz et al. 2021; Sabotta et al. 2021). From the 2700 or so confirmed planets in the Kepler field nearly one half are in multiple planetary systems. We achieve a match between the observed and simulated planet samples – both in terms of total planet number and

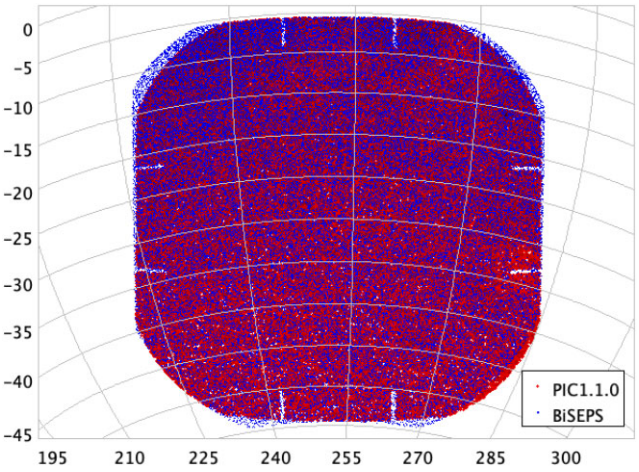

Figure 5. P5 target stars in the proposed Southern PLATO field as defined in the PIC 1.1.0 (red), overlaid with the locations of the P5 target stars identified in the synthetic southern PLATO field (LOPS0), used in this research (blue). Galactic longitude *x*-axis and Galactic latitude *y*-axis.

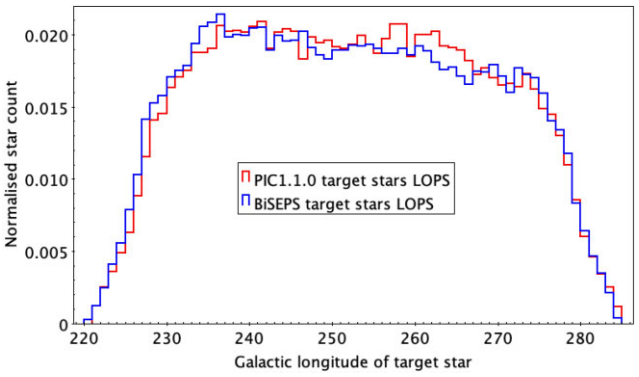

Figure 6. P5 target star distribution with Galactic longitude in the proposed Southern PLATO field as defined in the PIC 1.1.0 (red), and in the synthetic southern PLATO field LOPS0 (blue).

in relative distribution over planet radius and planet orbital period – by applying an overall scaling factor of 1.5 to the synthetic sample after the *P* and *R* adjustment described above. Again readers wanting more detail are directed to Rowden (2018).

4 ANALYSIS OF THE LOPS

4.1 The proposed LOPS (LOPS0)

The LOP fields are not simple geometric shapes so for simplicity of analysis, we have used Galactic coordinates to simulate a square field on the celestial sphere and then shaped the field using an elliptical approximation for each of the four detector groups. While not exact, the resulting synthetic LOPS0 shape and camera overlap pattern centred on $l = 253^\circ$ and $b = -30^\circ$ provides a very good approximation to the LOPS area analysed in PIC1.1.0. A comparison of the LOPS0 area in PICtarget110 and the synthetic LOPS0 area created by this technique is shown in Fig. 5 with the normalized target star numbers by Galactic longitude and latitude shown in Figs 6 and 7, respectively.

The synthetic LOPS0 is created by combining simulations of sub-fields of one degree by one degree in *l* and *b*. For simplicity, we use

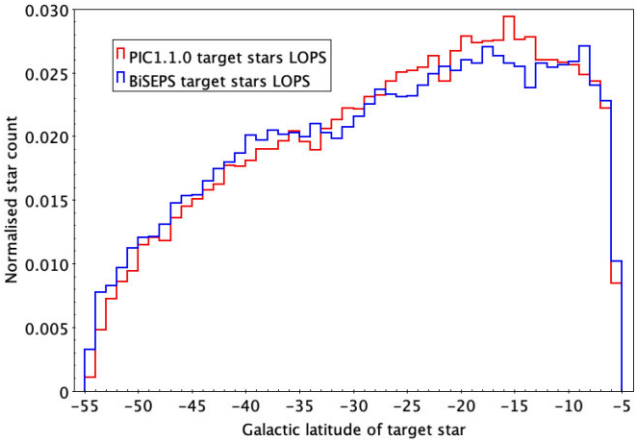

Figure 7. As Fig. 6, but for Galactic latitude.

lines of constant Galactic latitude ($b = -5.5^\circ$ and $b = -53.5^\circ$), as the upper and lower bounds of our synthetic LOPS0, however, since the width of one degree in *l* reduces with increasing $|b|$, the number of sub-fields analysed at higher $|b|$ was increased according to the Haversine formula.

The simulation is CPU-time intensive and to make such a task manageable, we have utilized the parallel computing power of the Open University's CentOS7 computer cluster to systematically step through the large number of sub-fields.

To verify that our synthetic LOPS0 target population is representative of the observed population, we carried out a comparison of the number of target stars in the synthetic LOPS0 to that in PICtarget110. After removing objects in PICtarget110 with no $T_{\rm eff}$ values, we obtain a total of 140 105 objects with magnitudes $3 \leq G_v \leq 13$ and temperatures of 4065 K $\leq T_{\rm eff} \leq$ 6848 K. Our single star target population for the same magnitude and $T_{\rm eff}$ range contains 76 026 objects. The analysis of the *Gaia* DR2 catalogue by Arenou et al. (2018) suggests that within 1 arcsec of an object, the catalogue is only ∼75 per cent complete and does not exceed ∼90 per cent until separations of greater than 1.5 arcsec are reached. Hence there is a high likelihood that PICtarget110 contains a number of objects, observed as single stars, that our analysis would identify as binary star systems. If we make the first-order assumption that any binary system in our synthetic LOPS0 with an angular separation of 1 arcsec or less will not be resolved by *Gaia* this increases our target star list by 64 230 to 140 256 objects which is in very good agreement with the number in PICtarget110.

As can be seen in Figs 6 and 7 both the longitude and latitude distributions for the P5 target stars are well reproduced by the BiSEPS population synthesis.

For the first step of our synthetic LOPS0 analysis, we examine each 30 arcsec × 30 arcsec PLATO superpixel as outlined in Section 3. Examining only these superpixels reduces the analysis area by approximately 50 per cent at low Galactic latitudes ($b = -6^\circ$) and by approximately 90 per cent at mid-Galactic latitudes ($b = -45^\circ$).

4.2 Planet transit analysis

This analysis is carried out as follows: we seed every single star (i.e. every stellar source consisting of one star only) in the PLATO superpixels with one planet according to the intrinsic radius and period distribution derived in Section 3.4. In addition to selecting a planet radius and period, each planet is assigned a random orbital inclination angle. If this angle exceeds the critical inclination angle

Table 1. Variables used in total noise calculation in Section 4.2. Key: ppm = parts per million, e− = electrons, ADU = analogue to digital unit, s = second. The values for BGN, exposure time, and inverse-gain were obtained from proprietary PLATO mission documentation while readout and jitter noise were obtained from private communications with members of the PLATO Instrument Signal and Noise Budget team.

Item	ID	Value	Unit
Background noise	BGN	100	e−/ pixel/s
Readout noise	RON	57.7	e−
Inverse-gain	G	25	e−/ADU
Jitter noise	JN	9	ppm
Exposure time	$T_{\rm exp}$	21	s

(signifying a transit), the stellar properties, planet radius, orbital period and orbital inclination are added to the planet transit master file. This creates a master list of all planet transits in the synthetic LOPS0 superpixels. From this master file, we select single stars with a magnitude $m_v \leq 13$ and with effective temperatures between 3875 and 6775 K as the PLATO P5 target star group (Rauer & Heras 2018).

The final observable apparent transit depths are calculated by blending the synthetic transit depths with the total flux from the PLATO superpixel containing the target star. We adopt this approach to approximate the binary mask suggested by Marchiori et al. (2019) as the optimal solution for P5 targets.

To evaluate the detectability of a transit we use a simple representation of the main characteristics of the PLATO detector and merely determine if the transit depth is larger than the expected noise. A more sophisticated appraisal of the detector and the pipeline processes for extracting transits is beyond the scope of this global study.

We use the standard CCD equation as a simplified model to calculate the interim instrument noise to signal ratio ($N/S_{\rm int}$), for a four pixel area per camera per exposure as below:

$$N/S_{\rm int} = \frac{\sqrt{F_\star + (4 \times {\rm BGN}_{\rm flux} \times T_{\rm exp}) + 4 \times {\rm RON}^2 + \left(\frac{G^2}{3}\right)}}{F_\star}. \quad (2)$$

The estimated instrument values used for readout noise (RON), background noise (BGN), gain (G), and exposure time ($T_{\rm exp}$) are shown in Table 1. The BGN is approximated as a constant of 100 e-/pixel/s. BGN includes effects such as the contribution from the zodiacal light, and stray light from the Moon, Earth, and Sun. Ideally, this should be calculated for each superpixel. A much more in-depth analysis of the detector performance would be required for this which is well beyond the scope of this paper. BGN does not, however, include unresolved background stars as these are taken into account by virtue of the fact that the synthetic model extends to stars and binaries of 26th magnitude ($m_v = 26$), all of which are being added as de-facto contaminants to the target star flux. *RON* includes contributions from both the CCD and front end electronics which are added in quadrature. We assume that the point spread function extends over all four pixels of the PLATO superpixel. The values for exposure time, inverse-gain and readout noise were obtained from proprietary PLATO mission documentation and private communications with members of the PLATO Instrument Signal and Noise Budget team.

To calculate the total photon count, $F_\star$, from the target star received during the exposure, we use the $T_{\rm eff}$ of the target star and the *Planck* function to calculate its blackbody spectrum using the throughput by wavelength function shown in Table 2. We calculate the target star photon count per camera noting the known visual flux for an $m_v = 11$ star is 10 856 photons s^{-1} cm^{-2} nm^1 (Johnson 1966).

Table 2. Detector throughput used in total noise calculation Key: nm = nanometres. Estimates of throughputs by wavelengths obtained from private communications with members of the PLATO Instrument Signal and Noise Budget team.

Wavelength (nm)	Throughput
500	0.47
550	0.53
600	0.59
650	0.59
700	0.59
750	0.52
800	0.45
850	0.34
900	0.22
950	0.12
1000	0.04

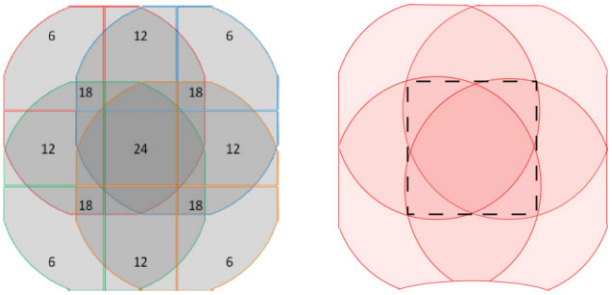

Figure 8. The left-hand panel shows the PICtarget110 FOV, and camera overlap pattern projected onto the celestial sphere (PLATO | Institut d'Astrophysique Spatiale)[2]. The right-hand panel shows the synthetic FOV and camera overlap pattern calculated in Galactic coordinates, also projected onto the celestial sphere. The boundary of the 18 camera overlap area used in PICtarget110 is shown in the right-hand panel by the dashed black lines.
[2]https://www.ias.u-psud.fr/en/technical-activities/optics-department/plato

The calculated $N/S_{\rm int}$ value is then combined in quadrature with a jitter noise approximation of 9ppm, and then since the cameras are cycling every 25 s, the $N/S_{\rm int}$ value for a 1-h integration is reduced further by $\sqrt{25/3600}$.

Our analysis shows that 90 per cent of target stars have a magnitude $m_v < 13$ and 80 per cent of FPs have a magnitude $m_v > 16$. This means that in a 'worst case' type scenario where a target star has an $m_v = 13$ and a contaminant has a magnitude of $m_v = 16$ the effect of adding the background flux into the noise equation would reduce the transit depth by less than 3 per cent. Further, both the PT and FP analysis would be subject to the same noise which would effectively cancel out leaving the per centFP ratio virtually unchanged. As a result, we deem the effect of the background flux negligible and we exclude it from our noise calculation.

Finally, we calculate the number of observing cameras assuming all cameras are functional, so each group contains six cameras.

As shown in Figs 5 and 8, the camera coverage and overlap pattern we calculate in Galactic coordinates, provide a good approximation for the FOV used in PICtarget110 with the difference in area being less than 2 per cent.

For simplicity, the synthetic FOV interior camera group boundaries are approximated as ellipses in Galactic coordinates which closely resemble the observed circular areas when converted to the 'on-sky'

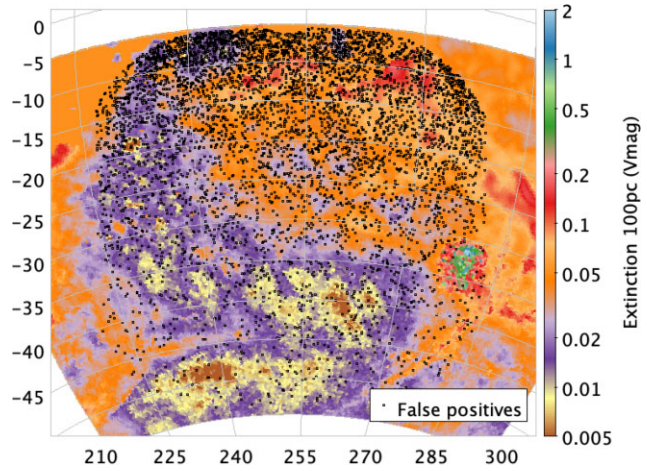

Figure 9. The Drimmel extinction map showing extinction, in *V* magnitude, at 100 pc with FP locations in the default Southern PLATO field (LOPS0), overlaid in black. Galactic longitude *x*-axis and Galactic latitude *y*-axis.

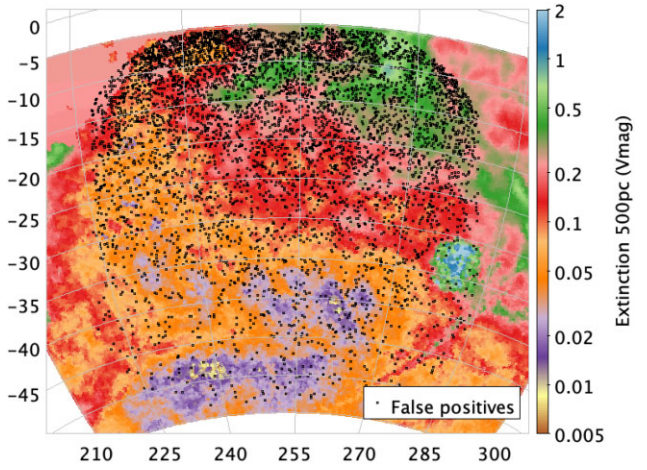

Figure 10. The Drimmel extinction map showing extinction, in *V* magnitude at 500 pc, with FP locations in the Southern PLATO field (LOPS0), overlaid in black. Galactic longitude *x*-axis and Galactic latitude *y*-axis.

view. While this results in a slight difference between the area where 18 cameras overlap at the expense of the area where 12 cameras overlap when compared to PIC110 area, the discrepancy is less than 3 per cent. The boundary of the PIC110 18 camera overlap area is shown by the dashed black line in the right-hand panel of Fig. 8.

We then compare each target star coordinate with each camera group coverage area to calculate the number of camera groups ($N_{\rm cg}$) observing the transit. The $N/S_{\rm int}$ value is then further reduced by $1/\sqrt{N_{\rm cg} \times 6}$ to give a final N/S value.

A planetary transit is recorded if the observed transit depth (flux from the star out of transit minus the flux from the star mid-transit), when blended with the total flux from the PLATO superpixel, exceeds the corresponding detector N/S value calculated above. This is the same threshold we use for FPs resulting from eclipsing binaries. While a 1σ detection threshold seems optimistic, we find that introducing a higher threshold has little influence on our results (see Section 4.5 for more detail).

The detections are binned in a 2D, matrix according to apparent planet radius (R), and orbital period (P), with this number then multiplied by the normalization factor of 1.5 obtained in Section 3.4. The seeding process is repeated 15 times and the results averaged. The standard deviation from the 15 simulations is then used as an estimate for the uncertainty for each planet apparent radius/period bin combination.

4.3 Eclipsing binary analysis

For the eclipsing binary analysis, we again interrogate the LOPS0 superpixels. For each target star (regardless of whether there is a planet transit or not, and there may be multiple target stars in a superpixel), we select an area around the target star of 30 arcsec × 30 arcsec and identify every single star and binary system down to 26th magnitude. We then assign each binary system in this area a random orbital inclination angle and if this angle exceeds the critical orbital inclination angle (signifying an eclipse), the primary and secondary eclipse depths are calculated utilising the JKTEBOP code (Southworth et al. 2004, 2005, 2007) which includes quadratic limb darkening of Wade & Rucinski (1985). Finally, we determine the apparent eclipse depth for every eclipse from the reduction of the total superpixel flux during the respective eclipse, and record the corresponding planet mimic radius.

By using the BISEPS population files we are able to ensure the 4-pixel mask is universally applied so that even target stars on the very edge of the superpixel have a full 30 arcsec × 30 arcsec area analysed for eclipsing binaries.

We identify the deepest eclipse depth and if this exceeds the detector noise calculated in Section 4.2, the FP planet period and mimicked apparent radius is calculated. There may be multiple target stars and multiple background eclipses in each superpixel and each is analysed separately. Once again, the process is repeated 15 times and the results averaged with the standard deviation from the 15 simulations used as the uncertainty for the FPs in each apparent planet radius/period bin combination. For the purposes of our analysis, we exclude eclipses where only part of the disc of the eclipsing star transits its binary companion. Since we only consider non-grazing planet transits in our detections, we similarly only consider non-grazing eclipsing background binaries in our FP analysis. Distinguishing between grazing PTs and grazing binary eclipse light curves is not a trivial exercise and while the most sharply 'V' shaped transit curves will be determined to be grazing eclipsing binaries, there are very few circumstances where this can reliably be done by visual inspection only.

4.4 Extinction

Extinction is calculated following Drimmel, Cabrera-Lavers & López-Corredoira (2003), who use a 3D dust model scaled from *V*-band line-of-site extinctions utilizing data from the COBE/DIRBE near-infrared (NIR) instrument. The effect of high extinction in the region of Galactic coordinates $l = 280^\circ$ and $b = -32^\circ$ is reflected in the reduced number of FPs shown in Figs 9 and 10.

4.5 Results for LOPS0

The results of our analysis of the synthetic LOPS0 field are shown in Tables 3 and 4 and Figs 11 and 12. For ease of presentation, the period data was combined so the per centFP incorporates all periods from $-0.4 < \log(P/\mathrm{d}) \leq 3.2$. The per centFPs were calculated on a simulation by simulation basis to give a set of 15 per centFPs for each apparent planetary radius, these were then averaged and the standard deviation calculated to provide an estimate of the uncertainty in each

Table 3. PTs, FPs, and per centFP ((FP/(FP + PT))×100) in the default Southern PLATO field (LOPS0) for planet radii $0.2 < \log(R/\mathrm{R}_\odot) < 0.8$ and for detection thresholds of signal > noise and signal > 5 × noise.

Planet radius $\log(R/\mathrm{R}_\odot)$	−0.2, 0.0	0.0, 0.2	0.2, 0.4	0.4, 0.6	0.6, 0.8
PT (S > N)	108.0	441.2	782.8	503.8	114.1
FP	2.2	13.2	29.7	39.4	33.5
per centFP	1.9	2.9	3.7	7.3	22.9
PT (S > 5N)	0.7	12.5	90.4	188.4	84.7
FP	0.0	0.3	2.1	11.2	20.9
per centFP	–	3.9	2.2	5.7	20.0

of the per centFP values. Both PT and FP detections are based on signal greater than noise.

In Fig. 11, the large per centFP value and error bar for planets with $-0.4 < \log(R/\mathrm{R}_\oplus) \leq -0.2$ is a result of detections in only four of the 15 simulation runs and in one of those runs there was no planet detections hence the per centFP was 100 per cent.

Generally, we find a low per centFP in the main region of interest, namely the planets with $-0.2 < \log(R/\mathrm{R}_\oplus) \leq 0.4$. Furthermore our research suggests that FPs with periods between 180 and 1000 d are rare, representing only ∼2.6 per cent of the FP numbers.

The per centFP by planet radius bin (Table 4), shows that in the $-0.2 < \log(R/\mathrm{R}_\oplus) \leq 0.4$ range, the per centFP does not exceed 4 per cent.

While we show the number of PTs and FPs in our analysis we believe the per centFP ratio is a much more robust statistic to base our results on. To illustrate the effect of a higher detection threshold and the robustness of our per centFP ratio, we show in Table 3 the relative differences in FPs, PT, and per centFP using our selected threshold of signal > noise and a second detection threshold where only detections with a signal > five times the noise were recorded. We show the results for the planet radius bins $-0.2 < \log(R/\mathrm{R}_\odot) < 0.8$ and we can see that while the FPs reduce significantly so too do the PTs resulting in a much smaller change, of at most a factor of 2, in the per centFP ratio.

5 TREND ANALYSIS OF THE SYNTHETIC LOPS0

To identify trends in PTs, FPs, and per centFPs, we subdivide the synthetic LOPS0 field into strips which, for ease of reference, we refer to as 'horizontal' and 'vertical'. For both the horizontal and vertical strip analysis, we ignore the detector shape and camera overlap pattern, instead we create rectangular sub-fields of equal area and assign each to be observed by two camera groups.

For the horizontal strips, we subdivide our 48° Galactic latitude LOPS0 field into 12 strips, each covering 4° in Galactic latitude. We dynamically set the Galactic longitude boundaries for each latitude setting so that each 1° latitude sub-strip covers an area of 50 square degrees, giving a total area for each horizontal strip of 200 square degrees.

For the vertical strips, we work from the centre of the field outwards, setting the inner boundaries of the first two strips at the Galactic longitude $l = 253°$. We then dynamically set the outer Galactic longitude boundaries for each latitude setting in the strip so that each 1° latitude strip covers an area of 5 square degrees.

The process is then repeated with subsequent strips starting where the previous ones ended so that no strip overlaps another, resulting in a total area for each strip of 240 square degrees.

For both the horizontal and vertical strips, we set the lower boundary at the Galactic coordinate $b = -5.5°$ and the upper boundary at $b = -53.5°$. To remove the confounding effect of increased resolution from the overlapping camera pattern, we arbitrarily assign each subfield to be observed by two camera groups.

For each vertical and horizontal strip, we calculate the PTs, FPs, and per centFPs by planet radius bin as described in Sections 4.2, 4.3, and 4.5, respectively.

We use least-squares analysis to calculate the best-fitting parameters for linear, exponential, and second-order polynomial functions and finally select the overall best-fitting function according to the Bayesian information criteria (BIC). For our BIC calculations, the likelihood is calculated using chi-squared. Uncertainties in our best-fitting functions are calculated as the mean of the least-square residuals, $\sqrt{\Sigma(x-\overline{x})^2/N}$. The result of this analysis is shown in Table 5.

5.1 LOPS0 – analysis of strips of constant longitude

We first discuss the vertical strips which allow us to probe the longitude dependence of the FP rate across the LOPS0 field.

As shown in the 'V' strips section in the LHS of Table 5, there is only a single instance where a polynomial fit is preferred over linear or exponential fits and its preference is insignificant.

The remaining best fits were predominantly exponential with six instances where the linear functions were preferred. However, we note that the preference of one distribution over the other two is very weak in all cases.

To highlight the magnitude of the change of per centFP with Galactic longitude l, we calculate the change in PTs, FPs, and per centFPs, per 50° of l using the best-fitting equations.

A graphical representation of the results for the vertical strip analysis for the three radius bins covering the radius range $-0.2 < \log(R/\mathrm{R}_\oplus) \leq 0.4$, are shown in the left-hand panels of Fig. 12.

Considering the trend across the 50° Galactic longitude step calculated above, we find a modest **negative** correlation across all the radii bins between the number of PTs and increasing l amounting to no more than ∼ 3 per cent across the 50° step. For the FPs, we find a modest **positive** correlation between the number of FPs and increasing l, again amounting to no more than ∼3 per cent across the 50° step. To test this correlation, we calculated the best-fitting flat-line (i.e. no correlation between l and the per centFP), for the planet radius bins $-0.2 < \log(R/\mathrm{R}_\odot) < 0.8$. Table 7 shows that for the radius range analysed, the exponential best-fitting function is only marginally preferred over the flat-line best fit. Analysing the best-fitting and the flat-line best-fitting functions using the Bayesian information criteria (ΔBIC), we find no evidence for the exponential function to be preferred over a flat per centFP value for the radius bins $0.0 < \log(R/\mathrm{R}_\odot) < 0.6$ and only a slight preference for the exponential best-fit function over the flat-line best fit for the other two radius bins.

We conclude that while there appears to be a weak positive correlation between the Galactic longitude l and the per centFP, and we would expect such a correlation as we move closer to the Galactic centre, this is not strongly favoured statistically over no trend.

5.2 LOPS0 – analysis of strips of constant latitude

We now turn to the horizontal strips that allow us to probe the latitude dependence of the FP rate as we move up the LOPS0 field.

For the PTs, FPs, and per centFPs there is again only one radius bin where a polynomial fit is preferred. Almost exclusively, the

Table 4. PTs, FPs, and per centFP ((FP/(FP + PT)) × 100) in the default Southern PLATO field (LOPS0).

Planet radius – log ($R/R_\odot$)	−0.4, −0.2	−0.2, 0.0	0.0, 0.2	0.2, 0.4	0.4, 0.6	0.6, 0.8	0.8, 1.0	1.0, 1.2
PT	7.2	108.0	441.2	782.8	503.8	114.1	44.8	41.8
FP	0.1	2.2	13.2	29.7	39.5	33.5	24.9	15.9
per centFP	7.1	1.9	2.9	3.7	7.3	22.9	35.7	27.7

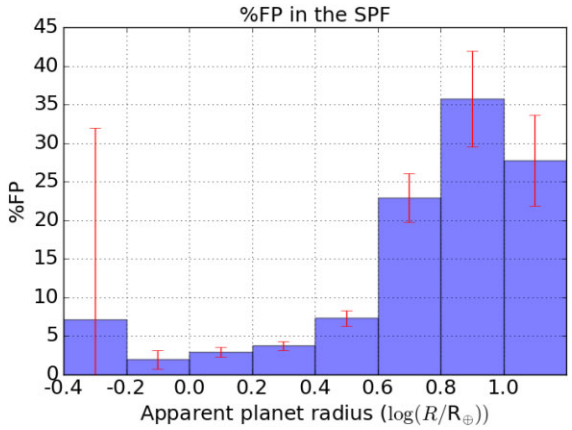

Figure 11. The per centFP, in the default southern PLATO field (LOPS0). Shown by apparent planet radius detected with data from periods in the range $-0.4 < \log(P/\mathrm{d}) \leq 3.2$ summed and with the per centFP shown as a percentage.

exponential distribution is preferred, and in most cases the preference for this distribution over the others is strong, especially for the per centFP data sets. As expected, we see a significant reduction in the per centFP with increasing $|b|$, as the stellar density reduces and the target background and foreground fields become less dense. We once again calculate the change in per centFP per 50°, this time for the Galactic latitude b using the best-fitting equations.

The magnitude of the change in per centFP is significant, with the decrease with $|b|$ being approximately 10 times the increase in per centFP for the corresponding radius bin. Of particular note is the significant increase in the per centFP in each radius bin in the region $|b| \leq 13.5°$ (refer to Table 6). A graphical representation of the results for the horizontal strip analysis for the three radius bins covering the radius range $-0.2 < \log(R/R_\oplus) \leq 0.4$, is shown in the right-hand panels of Fig. 12.

While the overall per centFP in the LOPS0 field is relatively low, the increase in the per centFP near the Galactic plane is significant. For the three bins of most interest, the average per centFP is approximately 13 per cent in the region $5.5 < |b| \leq 9.5°$.

While it is tempting to compare the dependence of the PLATO per centFP on Galactic longitude and latitude to what is seen for FPs in the Kepler field, a meaningful comparison is difficult without considerable analysis. This is mainly because the instrument characteristics are very different between Kepler and PLATO; in particular, Kepler's angular resolution is about four times better, and so most eclipsing binaries that give rise to FPs for PLATO are irrelevant for Kepler.

While such a detailed analysis is beyond the scope of this paper, we have carried out a basic analysis to calculate the approximate Kepler per centFP rate by Galactic latitude. We extracted the Kepler confirmed planets and FPs from the NExScI catalogue, limiting both data sets to a maximum Kepler magnitude $K_p < 13$, a maximum planet radius mimic of $\log(R/R_\odot) < 1.2$ and combining all periods. For the FPs, we consider only those identified as being a result of eclipsing binaries to match our synthetic analysis. We binned the per centFP into three bins, $9.5 < |b| \leq 13.5°$, $13.5 < |b| \leq 17.5°$, and $17.5 < |b| \leq 21.5°$, to match our synthetic data bins. For the synthetic per centFP, we have simply averaged the per centFP for the relevant latitude range shown in Table 6.

As can be seen from Table 8, we find that the trend of the per centFP with Galactic latitude in our synthetic SPF0 field is qualitatively consistent with that seen in the Kepler field. As expected from the difference in angular resolution, the per centFP seen in our synthetic PLATO field is higher than for Kepler. We reiterate that our analysis is only approximate and a more rigorous analysis would be required to confirm the match.

6 EXTRAPOLATION TO OTHER FIELD CENTRE LOCATIONS WITHIN THE ALLOWED LOPS REGION

Given the random nature of the orbital alignments, the more target stars that are observed the higher the expected number of planet detections. As a result, the prime reason for investigating the effect of different field centre coordinates on per centFP is to determine at what point the increased number of target stars observed by moving to a more crowded field, is negated by the increase in FPs resulting from more densely populated background and foreground fields.

Since our results are obtained from a synthetic population based on statistical distributions, and are subject to numerous simplifications and parametrizations of the input physics, we recognize that the simulated absolute number of PT and FP detections are subject to uncertainties and may well differ from the absolute number of future observed detections. However, by using a ratio of FP/(FP + PT), the effect of simplifications in the detector modelling and assumptions in the input physics is applied equally to the numerator and denominator and hence effectively cancel out.

To quantify the effect on the per centFP of moving the field centre location within the allowed region, we use the best-fitting per centFP distributions from the vertical strips to model the effect on the per centFP of changing the Galactic longitude of the field centre location while keeping the latitude constant. Similarly we use the best-fitting per centFP distributions from the horizontal strips to model the effect on changing the Galactic latitude of the field centre while keeping the Galactic longitude constant. For simplicity, where a region of LOPS0 crosses into the northern Galactic hemisphere we model the Galactic latitude using the corresponding Southern hemisphere latitude, i.e. the $b = +4°$ data sets are modelled using the best fits for $b = -4°$. We then scale the resultant per centFP by the relative combined area of the sub-fields and the synthetic LOPS0.

Uncertainties for each extrapolated point $\hat{y}(\hat{x})$ were calculated using $\sigma_{\hat{y}} = \sqrt{\frac{\sigma^2}{N} \times \left[1 + \left(\frac{\hat{x}-\bar{x}}{\sigma_x}\right)^2\right]}$.[2] While the Bevington & Robinson

[2] https://w3.pppl.gov/ hammett/work/1999/stderr.pdf

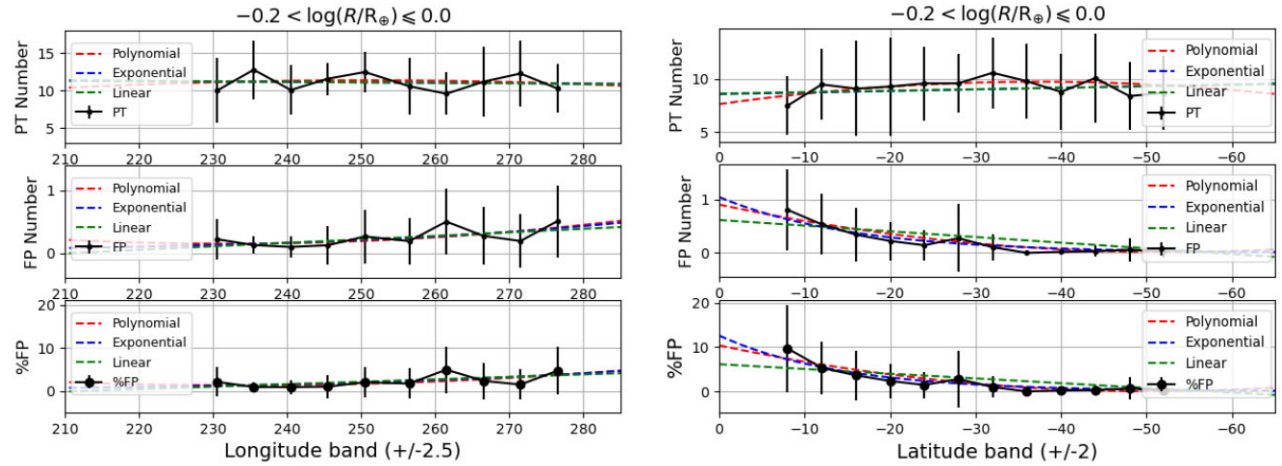

(a) Vertical strip - Planet radii : $-0.2 < \log(R/R_\oplus) \leqslant 0.0$

(b) Horizontal strip - Planet radii : $-0.2 < \log(R/R_\oplus) \leqslant 0.0$

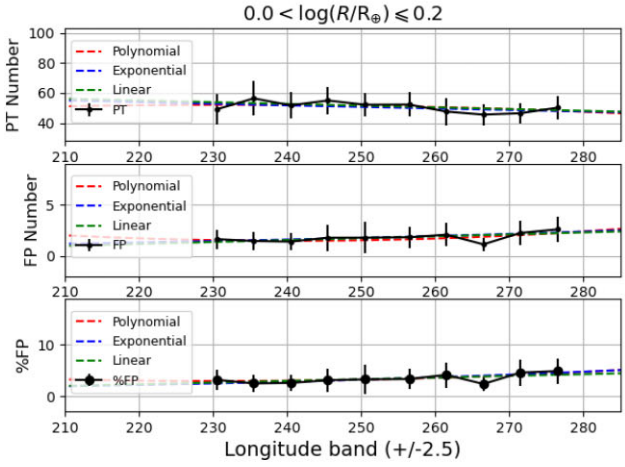

(c) Vertical strip - Planet radii : $0.0 < \log(R/R_\oplus) \leqslant 0.2$

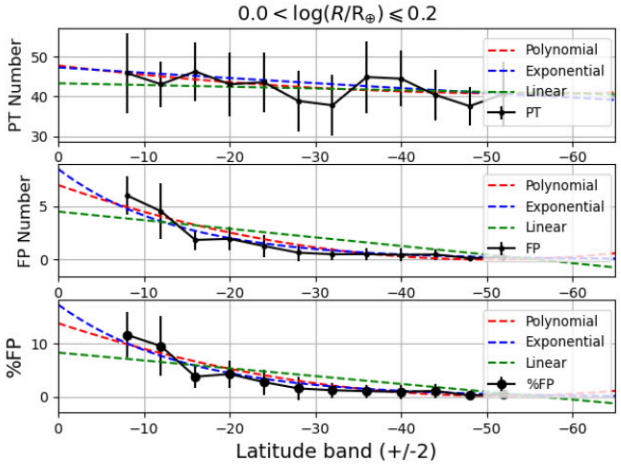

(d) Horizontal strip - Planet radii : $0.0 < \log(R/R_\oplus) \leqslant 0.2$

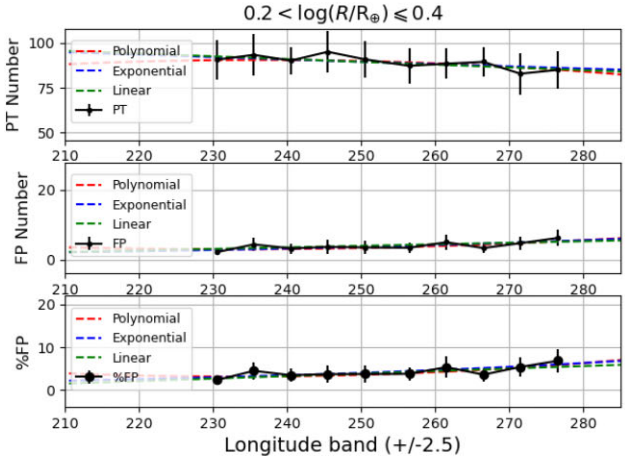

(e) Vertical strip - Planet radii : $0.2 < \log(R/R_\oplus) \leqslant 0.4$

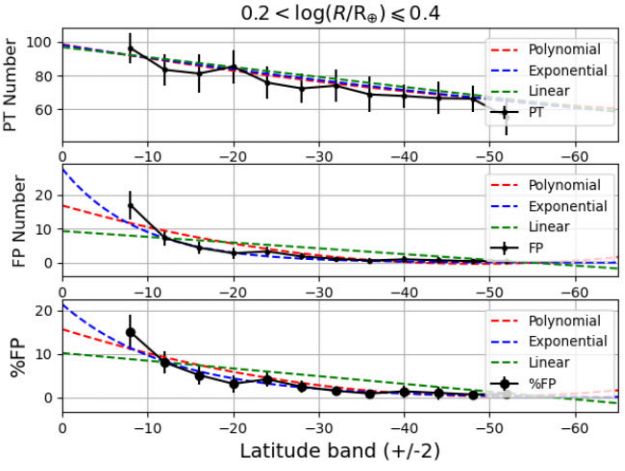

(f) Horizontal strip - Planet radii : $0.2 < \log(R/R_\oplus) \leqslant 0.4$

Figure 12. Comparison of 'vertical' and 'horizontal' strip analysis for the three strips covering the radius range $-0.2 < \log(R/R_\oplus) \leq 0.4$. The number of PTs, top panel, number of FPs, middle panel, and the per centFP ((FP/(FP + PT))×100) bottom panel. Plots (a), (c), and (e) show analysis of 'vertical' strips, plots (b), (d), (f) show analysis of 'horizontal' strips.

Table 5. Best-fitting variables for PT, FP, and per centFP data sets. (Lin = linear, Poly = polynomial, Exp = exponential, H = horizontal, V = vertical. Δ is the change of the variable over 50° longitude or latitude.).

Planet radii		V strip					H strip				
log(R/R$_\oplus$)	Data set	Best Fit	ΔBIC Poly	ΔBIC Exp	ΔBIC Lin	Δ (50°)	Best Fit	ΔBIC Poly	ΔBIC Exp	ΔBIC Lin	Δ (50°)
−0.4, −0.2	PT	Exp	0.60	–	0.01	−0.24	Exp	0.74	–	0.14	− 0.25
	FP	Exp	0.66	–	0.01	−0.01	Exp	0.58	–	4.11	− 19.55
	per centFP	Exp	0.75	–	0.27	−0.56	Poly	–	0.58	4.70	− 6.53
−0.2, 0.0	PT	Lin	0.95	1.43	–	+ 0.31	Lin	4.65	0.02	–	+ 0.91
	FP	Lin	2.36	0.43	0.08	+ 0.31	Exp	4.66	–	1.26	− 1.03
	per centFP	Poly	–	0.51	0.43	+ 2.83	Exp	2.74	–	12.55	− 12.50
0.0, 0.2	PT	Exp	1.02	–	0.08	−5.74	Lin	5.11	0.01	–	− 2.92
	FP	Exp	0.93	–	0.08	+ 0.94	Exp	4.14	–	15.09	− 8.48
	per centFP	Exp	1.02	–	0.08	+ 1.62	Exp	17.21	–	4.89	− 17.14
0.2, 0.4	PT	Lin	1.00	0.00	–	−7.71	Exp	5.16	–	0.36	− 41.57
	FP	Exp	0.26	–	1.31	+ 2.19	Exp	11.04	–	36.89	− 27.81
	per centFP	Lin	0.99	0.24	–	+ 2.92	Exp	3.45	–	18.74	− 21.36
0.4, 0.6	PT	Exp	0.97	–	0.15	−6.82	Exp	5.04	–	0.39	− 32.78
	FP	Exp	0.98	–	0.02	+ 2.59	Exp	14.92	–	52.51	− 27.10
	per centFP	Exp	1.04	–	0.10	+ 3.75	Exp	5.35	–	31.69	− 30.36
0.6, 0.8	PT	Exp	0.95	–	0.04	−1.36	Lin	4.91	0.25	–	− 6.41
	FP	Exp	0.89	–	0.02	+ 1.25	Exp	34.95	–	68.65	− 26.47
	per centFP	Lin	0.06	0.02	–	+ 7.60	Exp	29.78	–	46.54	− 67.94
0.8, 1.0	PT	Exp	1.12	–	0.00	−0.18	Exp	5.28	–	0.06	− 3.85
	FP	Exp	1.00	–	0.01	+ 0.03	Exp	13.72	–	49.08	− 17.32
	per centFP	Exp	0.90	–	0.02	+ 0.74	Exp	0.03	–	27.29	− 74.73
1.0, 1.2	PT	Exp	0.36	–	0.02	−0.22	Exp	5.22	–	0.02	− 2.74
	FP	Lin	1.01	0.03	–	+ 0.54	Exp	11.02	–	23.53	− 10.33
	per centFP	Exp	0.29	–	0.30	+ 8.36	Exp	17.60	–	31.64	− 65.78

Table 6. Percent of FP detections (per centFP), by Galactic latitude (b), in 'horizontal' strips in the default Southern PLATO field (LOPS0).

	Planet radius log (R/R$_\odot$)							
b°	−0.4, −0.2	−0.2, 0.0	0.0, 0.2	0.2, 0.4	0.4, 0.6	0.6, 0.8	0.8, 1.0	1.0, 1.2
−5.5, −9.5	27.07	11.48	12.07	14.92	23.02	57.31	68.64	59.83
−9.5, −13.5	0	5.65	9.26	8.19	15.18	36.93	54.35	46.10
−13.5, −17.5	6.67	9.92	3.78	5.27	9.22	23.16	41.62	36.32
−17.5, −21.5	6.67	3.13	4.46	3.14	6.77	15.67	40.99	22.15
−21.5, −25.5	0	1.14	2.79	4.21	5.49	15.40	32.51	18.52
−25.5, −29.5	0	2.00	1.49	2.52	3.34	8.85	28.28	19.99
−29.5, −33.5	0	0.93	1.17	1.56	2.80	11.94	17.42	40.26
−33.5, −37.5	0	0	1.25	0.88	1.89	8.16	12.49	7.63
−37.5, −41.5	6.79	0.32	0.87	1.40	2.03	8.59	29.28	18.30
−41.6, −45.5	0.21	0.22	1.05	1.06	1.70	12.91	17.42	22.26
−45.5, −49.5	0	0.40	0.32	0.65	1.59	3.30	24.41	21.97
−49.5, −53.5	0	0.24	0.54	0.78	1.11	2.97	3.35	1.83

Table 7. Best-fitting functions for per centFP for vertical strips compared to no trend (per centFP constant). σ_{res} is the mean of the residuals.

Planet radius log (R/R$_\odot$)	−0.2, 0.0	0.0, 0.2	0.2, 0.4	0.4, 0.6	0.6, 0.8
Best-fit percentFP	Exp	Exp	Exp	Exp	Exp
σ_{res}	0.35	0.20	0.26	0.33	1.06
per centFP = const	2.3	3.4	4.3	7.7	22.8
σ_{res}	0.44	0.26	0.38	0.53	1.31
ΔBIC	5.0	1.9	0.8	0.0	2.9

Table 8. Comparison of the per centFPs in the synthetic PLATO field versus those observed by Kepler.

Latitude range	PLATO SPF0	Kepler
9.5:13.5	22 per cent	18 per cent
13.5:17.5	17 per cent	14 per cent
17.5:21.5	13 per cent	7 per cent

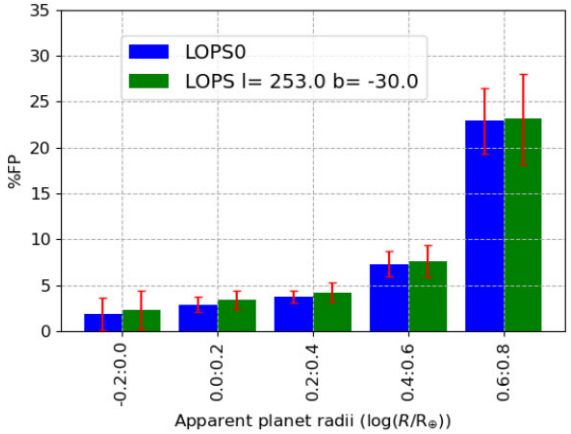

Figure 13. Comparison of the projected per centFP, by planet radius bin for LOPS0 ($l = 253^\circ$ $b = -30^\circ$). The blue bars show the LOPS0 per centFP using the camera coverage pattern shown in Fig. 8 and the green bars are the per centFP projected using **vertical** strip best-fitting equations for the LOPS0 field assuming the entire area is covered with two cameras.

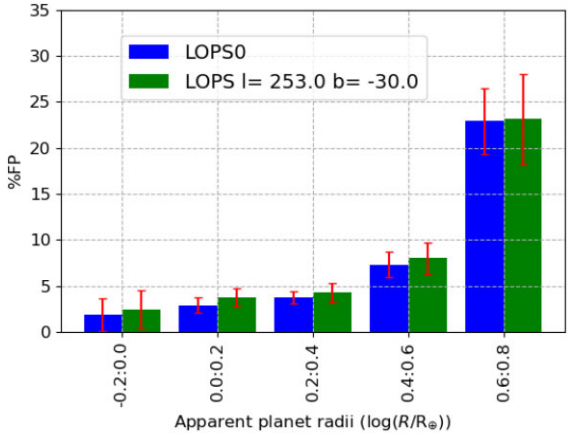

Figure 14. Comparison of the projected per centFP, by planet radius bin for LOPS0 ($l = 253^\circ$ $b = -30^\circ$). The blue bars show the LOPS0 per centFP using the camera coverage pattern shown in Fig. 8 and the green bars are the per centFP projected using **horizontal** strip best-fitting equations for the LOPS0 field assuming the entire area is covered with two cameras.

(2003) formula this equation is based on is for a linear fit, we believe, given the other uncertainties in our data, this provides an acceptable estimate for the uncertainties in the extrapolated points. The total uncertainties for each planet radius bin for the new field locations were obtained by combining the uncertainty in the per centFP in SPF0, the uncertainty in the best fit for the per centFP in SPF0 and each uncertainty in the extrapolated points using the sum of the squares.

In Fig. 13, we show the comparison between the predicted per centFP by apparent planet radii mimicked using the 15 LOPS0 simulations and camera overlap pattern shown in the right-hand panel of Fig. 8 (blue bars), and that obtained by combining the vertical strips (green bars), and scaling the area to match LOPS0. In Fig. 14, we show the same match this time using the horizontal strips. The approximation in the strip analysis of each FP, regardless of its location, being observed by two camera groups has little effect on the results, with the per centFP observed in the combined and scaled strips differing by no more than ≈1 per cent when compared to the results obtained using the LOPS0 shape and overlap pattern.

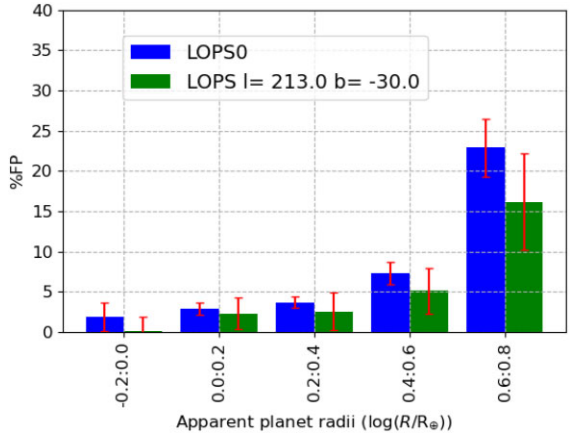

Figure 15. The projected per centFP, by planet radius bin when centre Galactic longitude only changes. Blue bars show the LOPS0 per centFP and the green bars are those projected per centFP for an LOPS field centre of $l = 213^\circ$ ($b = -30^\circ$).

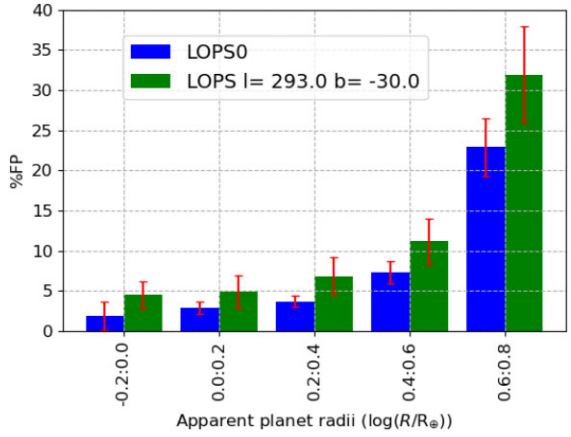

Figure 16. As per Fig. 15 but with green bars showing the projected per centFP for an LOPS field centre of $l = 293^\circ$ ($b = -30^\circ$).

Again we have excluded the smallest planet radius bin due to the small number statistics involved and exclude the two largest planet radius bins with $\log(R/R_\oplus) > 0.8$, as these are well outside the planet radius range of interest to the PLATO mission.

As expected, the effect on per centFP of changing the Galactic longitude l coordinate of the field centre location is minor with only a relatively modest change in the per centFP observed as the Galactic longitude l field centre location is moved away from, or towards, the Galactic centre by 40° (Figs 15 and 16, respectively).

As highlighted in Section 5, the effect of changing the field centre Galactic latitude b on the per centFP is far greater than changing the field centre coordinate galactic longitude l.

While we show the effect on per centFP for a field centre location of Galactic latitude $b = -42^\circ$ in Fig. 17, this is for completeness only as such a location would most likely be rejected as the total number of target stars observed in the two LOP fields is expected to drop well below the minimum requirement of 267 000 (Rauer et al. 2014).

In Figs 18 and 19, we show the effect of moving the field centre closer to the Galactic plane, galactic longitude $l = 253^\circ$ Galactic latitude $b = -18^\circ$ and Galactic longitude $l = 253^\circ$ Galactic latitude $b = -10^\circ$, respectively. As expected, these result in a significant

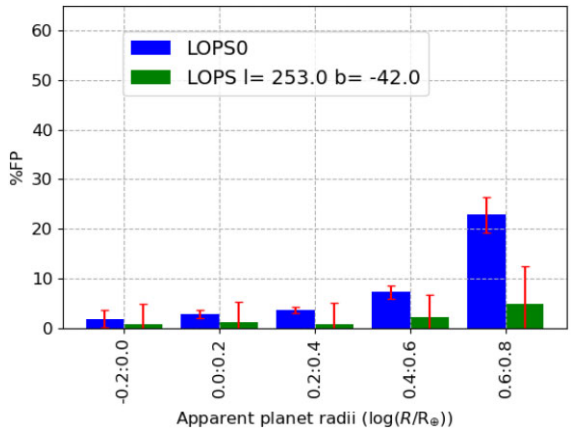

Figure 17. The per centFP, by planet radius bin when centre latitude only changes. Blue bars show the LOPS0 per centFP and the green bars are those projected for an LOPS field centre of $b = -42^\circ$ ($l = 253^\circ$).

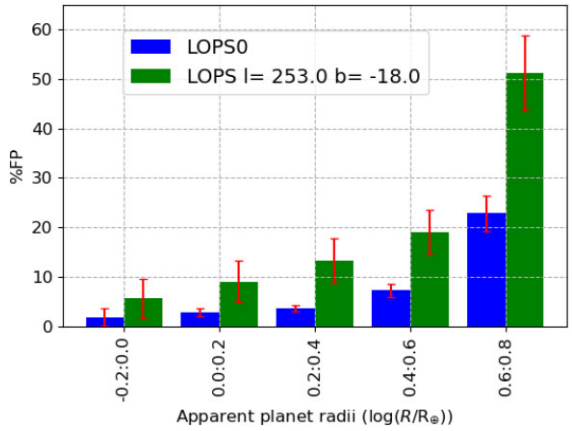

Figure 18. The projected per centFP, by planet radius bin when centre latitude only changes. Blue bars show the LOPS0 per centFP and the green bars are those projected for an LOPS field centre of $b = -18^\circ$ ($l = 253^\circ$).

increase in the per centFP. We note that a smooth Galactic density model is not likely to be representative of the actual population at very low latitudes and caution that statistics from locations of $|b| \leq 5^\circ$ need to be regarded as indicative only.

While the effect of moving both the Galactic longitude l and Galactic latitude b locations of the field centre could be modelled by averaging the effects of our two best-fitting functions, the averaging would introduce more uncertainty and given the small effect on the per centFP with changing galactic longitude l, such an exercise was not deemed to be beneficial.

7 COMPARISON TO LOPN AND PICTARGET110

We wish to compare our LOPS0 results with LOPN0. To this end, we rendered approximately 75 per cent of LOPN0 covering Galactic coordinates $l = 40.5^\circ$ to $l = 89.5^\circ$ and $b = 5.5^\circ$ to $b = 53.5^\circ$ which we call LOPN-sub. We create a comparable area in the LOPS covering $l = 228.5^\circ$ to $l = 277.5^\circ$ and $b = -5.5^\circ$ to $b = -53.5^\circ$ which we refer to as LOPS-sub. This enables us to compare and contrast the properties of these sub fields. A complete rendition of LOPN0 is time consuming and beyond the scope of this study.

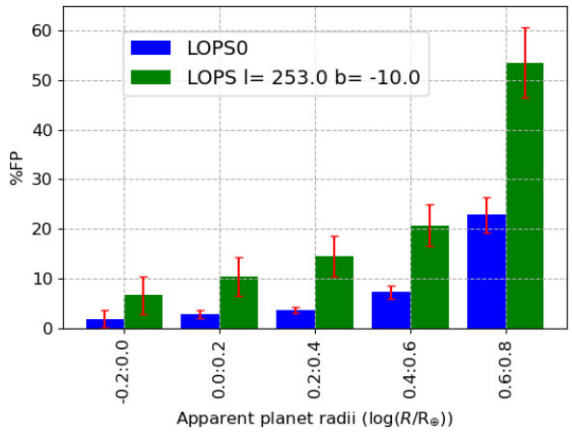

Figure 19. As per Fig. 18 but with green bars showing the projected per centFP for an LOPS field centre of $b = -10^\circ$ ($l = 253^\circ$).

Table 9. P5 target stars and unresolved binaries in PIC-LOPS-mini, PIC-LOPN-mini, LOPS-mini, and LOPN-mini.

Field	Single stars	Unresolved binaries	Total
PIC-LOPN-mini	51 563	–	51 563
LOPN-mini	23 559	25 079	48 638
PIC-LOPS-mini	47 486	–	47 486
LOPS-mini	24 947	26 113	51 060

7.1 Stellar populations

We first compare the P5 target star population of PICTarget110 to the corresponding regions in our LOPS-sub and LOPN-sub fields. To remove the effects of the PLATO detector geometry on the field shape we create sub fields from PICTarget110 and consider only the central region of the PICTarget110 northern and southern fields. We refer to these sub-fields as PIC-LOPS-mini and PIC-LOPN-mini. The synthetic fields matching the PIC-mini fields comprise approximately 30 per cent of the LOPs and cover $l = 243^\circ$ to $l = 263^\circ$ and $b = -9.5^\circ$ to $b = -53.5^\circ$ (LOPS-mini) and $l = 55^\circ$ to $l = 75^\circ$ and $b = 9.5^\circ$ to $b = 53.5^\circ$ in (LOPN-mini). Again for simplicity, we assume the entire area is observed by two camera groups.

As in Section 4.1, when we consider the unresolved binaries in our synthetic fields as target stars, we find a very good correlation between the target star numbers in PIC-LOPS-mini and LOPS-mini and between those in PIC-LOPN-mini and LOPN-mini. Both show variations of less than 10 per cent (see Table 9). While our synthetic fields show more target stars in LOPS-mini than LOPN-mini, which is the opposite of that seen in PIC-mini data sets, we again find less than 10 per cent variation which we believe is an acceptable variation given the approximations in the Galactic structure and input physics used in our simulations.

As well as an acceptable correlation between the target star numbers in the PIC and synthetic mini fields we compare the distance distribution of the target stars in PIC-mini and synthetic mini fields. Again, we find a good correlation with both the peak target star distance and overall distribution shape a good match (see Fig. 20).

7.2 PTs and FPs in the LOPS-sub and LOPN-sub fields

Returning to the LOPS-sub and LOPN-sub fields, we find a total of 1749 PTs in LOPN-sub compared to 1917 in LOPS-sub. Both PT and

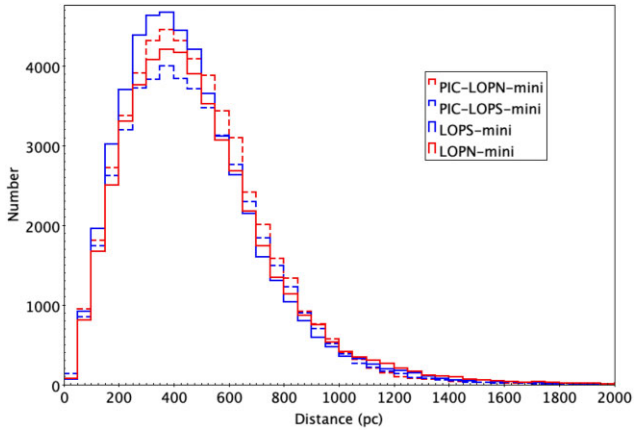

Figure 20. Comparison of target star distances in the smaller long duration observational field subsets – LOPS-mini solid blue line, LOPN-mini solid red line, PIC-LOPS-mini dashed blue line, and PIC-LOPN-mini dashed red line.

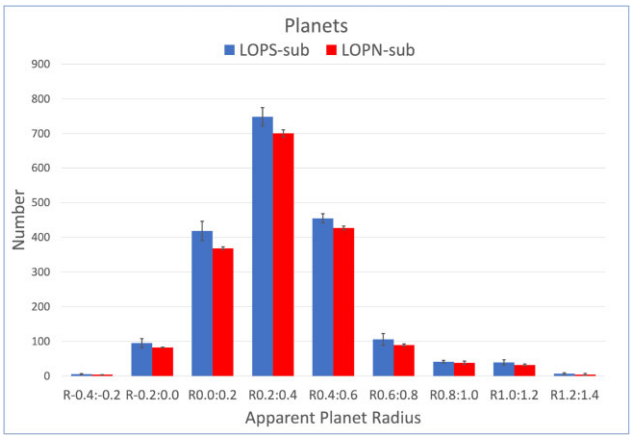

Figure 21. Comparison of planetary transit numbers (PTs) by radii detected in the long duration observational field south sub field (LOPS-sub) and the long duration observational field north sub field (LOPN-sub).

FP numbers were obtained by averaging results from five simulations with the error bars obtained from the standard deviations.

As shown in Fig. 21 despite the slight variation in PT numbers, we see a very similar apparent planetary radius distribution in LOPS-sub and LOPN-sub.

While the PT numbers in LOPS-sub and LOPN-sub are very similar the same cannot be said for the FP numbers. We find considerably more FPs in the LOPN-sub field as shown in Fig. 22.

The combined effect of slightly lower PTs and higher FPs in LOPN-sub results in a considerable higher per centFP in LOPN-sub than in LOPS-sub as shown in Fig. 23.

8 DISCUSSION AND CONCLUSIONS

In this work, we have used the BISEPS synthetic stellar models and population synthesis code to create a complete synthetic single and binary stellar population for LOPS0. The synthetic population was calibrated to reproduce the Kepler field content in $\log(g)$ versus $\log(T_{\rm eff})$ space, as well as the mass ratio and period distribution of Kepler-identified eclipsing binaries. We have verified that the number of synthetic single P5 target stars in the resulting synthetic LOPS0 is comparable to that in the PIC PICTarget110 when an estimate of the unresolvable binary population is added to the synthetic single star population and that the target star distribution by Galactic latitude and longitude is a good match to PICTarget110. Using the same calibration settings, we repeated the analysis for a subfield of the LOPN and again find a good correlation with PICTarget110 both in target star numbers and distance distribution. We reiterate that our FPs are those predicted from blended eclipsing binaries only and we do not consider other potential FP signals such as from stellar activity.

We seeded each single P5 target star in the synthetic LOPS0 super-pixels and in LOPN-sub super-pixels with a single planet whose number, radius and period distributions have been calibrated to reproduce the Kepler planet sample from the synthetic Kepler field.

We have analysed the resulting detectable PTs and FPs from blended eclipsing binaries and, using simplified specifications for the PLATO instrument, determined the FP rate by apparent planetary radius when each signal is blended with four PLATO pixels.

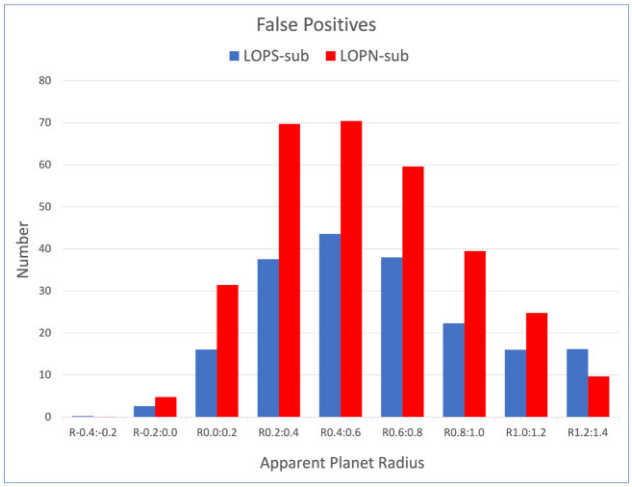

Figure 22. Comparison of FP planetary transit numbers (FPs) detected in the long duration observational field south sub field (LOPS-sub) and the long duration observational field north sub field (LOPN-sub).

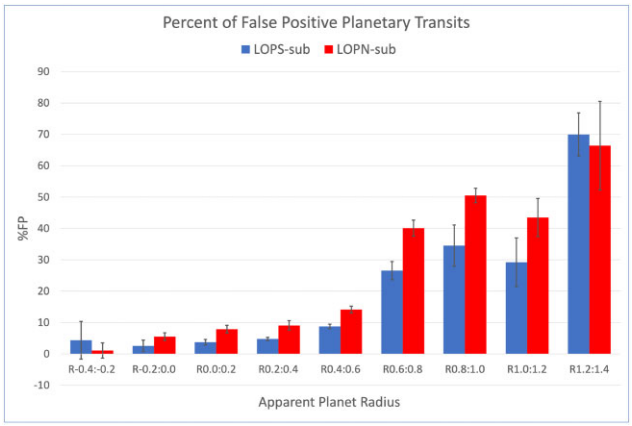

Figure 23. Comparison of FP PTs, in per cent, detected in the long duration observational field south sub field (LOPS-sub) and the long duration observational field north sub field (LOPN-sub).

8.1 LOPS

In the radius range of most interest to PLATO, $-0.2 < \log(R/R_\oplus) \leq 0.4$, we predict an average an FP rate of approximately 3 per cent from blended eclipsing binary systems in the LOPS0 field. However, we note a significant increase in the FP rate in regions of the LOPS0 where the absolute value of the Galactic latitude $|b| \leq 9.5^\circ$, and we show that most planetary radius bins in the synthetic LOPS0 would see a FP rate of at least 20 per cent for regions where Galactic latitude $|b| \leq 5.5^\circ$.

We split our synthetic LOPS0 into a number of equal area vertical and horizontal sub-fields to analyse the effect of varying the field centre Galactic longitude l or Galactic latitude b coordinates, respectively, on the PTs, FPs, and FP rate.

The vertical sub-field analysis indicates a modest increase in the FP rate with field centre longitude l. We obtain the best-fitting functions to model these trends and use these equations to estimate the FP rate expected for alternative longitude l field centre locations while keeping the latitude b field centre location constant. We conclude that the Galactic longitude of the field centre location within the LOPS allowed region does not significantly affect the FP rate from eclipsing blended binaries and as a result, conclude that, from the perspective of astrophysical FPs, the Galactic longitude choice is not a significant factor in the selection of the LOPS field centre.

Repeating a similar trend analysis on the horizontal strips and using the best-fitting functions to model the FP rate for alternative Galactic latitude b field centre locations while keeping the Galactic longitude l field centre location constant, we find a more significant increase in the FP rate with decreasing field centre latitude $|b|$. While this indicates a lower FP rate will be obtained with higher values of field centre latitude $|b|$, the number of target stars rapidly drops below the mission threshold of 267 000 assuming both the LOPS and the LOPN adopted higher b field centre locations. As a result, latitude pointings of $|b| \geq 30^\circ$ will most likely not be considered.

For field centre latitude pointings of $|b| \leq 30^\circ$, our research suggests that while the FP rate increases significantly, the overall rates are still likely to be less than ∼15 per cent for the planetary radius bins in the range $-0.2 < \log(R/R_\oplus) \leq 0.4$ even for a field centre location of $b = -10$.

This suggests that moving the field centre location to regions where Galactic latitude $|b| < 30^\circ$, would be advantageous for the planet radius range of most interest, namely $-0.2 < \log(R/R_\oplus) \leq 0.4$.

The effect of field centre latitude pointings of Galactic latitude $|b| < 30^\circ$ on larger planets is much more significant and we estimate that over 80 per cent of **additional** transit detections in the region of $|b| \leq 5.5^\circ$ in the radius range $\log(R/R_\oplus) > 0.6$ would be FPs.

We highlight that splitting the synthetic LOPS0 into sub-fields has resulted in some radius bins having very low counts for FPs, and this has resulted in increased uncertainties in the FP rate results especially for the smallest planetary radius bin $-0.4 < \log(R/R_\oplus) \leq -0.2$. As a result, we generally exclude this bin from our discussion but show the strip analysis results in Table 5 for completeness.

Our intrinsic planet distribution has been calibrated to match the Kepler confirmed planets using an approximation of the Kepler instrument properties. As a result, we believe our planet detection rates for PLATO using an approximation of the PLATO instrument properties provides a good 'order of magnitude' estimate for the expected planet detections. In the case of FPs from eclipsing binary systems, we constructed a BISEPS synthetic stellar population tailored to reproduce the Kepler target list in $\log T_{\rm eff}$ and $\log(g)$ space, used an approximation of the Kepler instrument properties, and then modified the resultant eclipsing binary period distribution to once again match the observed Kepler eclipsing binary data. While we believe both our resulting planet detections and FP rates provide reasonable approximations for each data set, our focus is on differential analysis of the per centFP rate with varying Galactic latitude and longitude both within the suggested PLATO field, and then for varied locations of the field within the allowed regions. Therefore we have focused our analysis on the differential change in the FP rates (per centFP), which we believe is a more robust statistic. This is because using a ratio of FP/(FP + PT), the effect of simplifications in the detector modelling and assumptions in the input physics is applied equally to the numerator and denominator and hence effectively cancel out. As a result, we caution against any inferences made using our PT and FP numbers alone.

Our method of calculating the transit and the eclipse depths by blending them with the flux from the super-pixel containing the target star is only an approximation of the method suggested in Marchiori et al. (2019). Their research suggests that both the number and location of the pixels used in the mask will depend on the point spread function, of the target star. Such an analysis is beyond the scope of this paper.

We have not attempted to model the detector in detail, rather, using a standard CCD equation and adopting realistic approximate noise values and throughputs, we have calculated an estimate for what might be expected which we deem broadly representative of the detector characteristics.

As shown in the example of changing the detection threshold in Section 4.5, while the FPs show a reduction of ≈ 97 per cent in the planet bin $0.0 < \log(R/R_\oplus) \leq 0.2$, for example, the reduction in PTs in the same bin is similar (a reduction of ≈ 98 per cent), resulting in a similar ratio. (Note that we are **not** suggesting the PLATO data processing pipeline should use a 1σ detection threshold. Rather, that in the region of planet radii of most interest to the PLATO mission $[-0.2 < \log(R/R_\oplus) \leq 0.4)$, we find that the detection threshold has little effect on the overall value of the per centFP calculated using our simulations.]

The main goal of our study is to explore the differential change of the FP rate (per centFP) with varying Galactic latitude and longitude, both within the suggested PLATO field and then for varied locations of the field within the allowed regions. The differential change of per centFP, we observe in our simulations is a more robust prediction than the magnitude of the FP rate, while per centFP in turn is a more robust result than the simulated absolute numbers of FPs and transiting planets in our model.

8.2 LOPN

While a full comparison of the LOPN field similar to that carried out for LOPS was beyond the scope of this study, the analysis of a significant portion of the LOPN sub-field suggests PLATO can expect a considerably higher FP rate in LOPN compared to the LOPS. This increase is a result of two factors, firstly we find slightly fewer target stars in the LOPN and secondly we find more FPs in the LOPN. While the lower number of target stars in LOPN is at odds with PICtarget110, the variation is not significant and is most likely an artefact from our simplified double disc Galactic structure. Of more significance is the greatly increased number of FPs in LOPN. While this is also driven by our synthetic Galactic structure model, the background in LOPN compared to the LOPS is observably more dense than the LOPS due to the LOPN being oriented more toward

the Galactic centre. This is supported by the PICcontaminant110 data set which shows approximately 36 per cent more contaminants in the LOPN than the LOPS. (Montalto et al. 2021).

8.3 Conclusions

Our research indicates that the per centFP from blended eclipsing binaries using the current proposed LOPS centre location of $b = -30^\circ$ and $l = 253^\circ$, is relatively low with an average of approximately 3 per cent in the radius range of most interest namely $-0.2 < \log(R/R_\oplus) \leq 0.4$. However, our research suggests that moving the field centre location closer to the Galactic centre to include targets with $|b| \leq 5.5^\circ$ will result in a significant increase in the per centFPs especially in the radius range $\log(R/R_\oplus) > 0.6$ where we expect that on average more than 80 per cent of additional detections will be FPs. For the LOPN, moving the field centre location closer to the Galactic plane will result in virtually all additional planet detections in the radius range $\log(R/R_\oplus) > 0.6$ being FPs.

Countering this increase, we find that only approximately 2.6 per cent of the identified fully eclipsing FPs have periods between 180 and 1000 d, resulting in the vast majority of the FPs identified being discounted as PTs of Earth-like planets around Sun-type stars due to their short periods. If the focus is purely on Earth-like planets orbiting Sun-type stars, moving the LOPS field centre closer to the Galactic plane should result in more target stars and more planet detections but the compromise will be significantly more FPs for shorter period planet transits and larger radius planets.

The difference in FP rates for LOPN and LOPS suggests that, from an astrophysical FP perspective, the LOPS would be a more productive field and consideration should be given to dedicating more of the initial 4-yr observational window to the southern field.

ACKNOWLEDGEMENTS

The authors would like to thank the anonymous referee for their thorough analysis and insightful suggestions which enabled us to significantly improve the paper.

This work presents results from the European Space Agency (ESA) space mission PLATO. The PLATO payload, the PLATO Ground Segment and PLATO data processing are joint developments of ESA and the PLATO Mission Consortium (PMC). Funding for the PMC is provided at national levels, in particular by countries participating in the PLATO Multilateral Agreement (Austria, Belgium, Czech Republic, Denmark, France, Germany, Italy, Netherlands, Portugal, Spain, Sweden, Switzerland, Norway, and United Kingdom) and institutions from Brazil. Members of the PLATO Consortium can be found at https://platomission.com/. The ESA PLATO mission website is https://www.cosmos.esa.int/plato. We thank the teams working for PLATO for all their work.

UK acknowledges support by STFC grant ST/T000295/1.

This research was supported by UKSA grant ST/R003211/1 (Open University element of PLATO UK – Support for the Development Phase)

JCB acknowledges the support provided by the University of Auckland and funding from the Royal Society Te Apārangi of New Zealand Marsden Grant Scheme.

DATA AVAILABILITY

Data available on request from the authors.

REFERENCES

Abdul-Masih M. et al., 2016, ApJ, 151, 101
Arenou F. et al., 2018, A&A, 616, A17
Batalha N. et al., 2010, ApJ, 713, L109
Bevington P., Robinson D., 2003, Data Reduction and Error Analysis for the Physical Sciences, 3rd edn. McGraw-Hill Education, Boston, MA
Brown T. M., Latham D. W., Everett M. E., Esquerdo G. A., 2011, ApJ, 142, 112
Cassan A. et al., 2012, Nature, 481, 167
Chen B. et al., 2001, ApJ, 553, 184
Conroy K. E. et al., 2014a, PASP, 126, 914
Conroy K. E., Prša A., Stassun K. G., Orosz J. A., Fabrycky D. C., Welsh W. F., 2014b, ApJ, 147, 45
Davis P. J., Kolb U., Willems B., 2010, MNRAS, 403, 179
Drimmel R., Cabrera-Lavers A., López-Corredoira M., 2003, A&A, 409, 205
ESA-SCI, 2017, Technical report, Definition Study Report (REDBOOK). ESA
Farmer R., Kolb U., Norton A. J., 2013, MNRAS, 433, 1133
Feliz D. L., Plavchan P., Bianco S. N., Jimenez M., Collins K. I., Villarreal Alvarado B., Stassun K. G., 2021, ApJ, 161, 247
Gilmore G., Wyse R. F. G., Jones B. J., 1995, ApJ, 109, 1095
Haywood M., 2001, MNRAS, 325, 1365
Heller R., Harre J.-V., Samadi R., 2022, A&A, 665, A11
Hurley J. R., Pols O. R., Tout C. A., 2000, MNRAS, 315, 543
Hurley J., Tout C., Pols O., 2002, MNRAS, 329, 897
Johnson H. L., 1966, ARA&A, 4, 193
Kirk B. et al., 2016, ApJ, 151, 68
Koch D. G. et al., 2010, ApJ, 713, L79
Kroupa P., Tout C., Gilmore G., 1993, MNRAS, 262, 545
LaCourse D. M. et al., 2015, MNRAS, 452, 3561
Marchiori N. V. et al., 2019, A&A, 627, A71
Matijevig G., Prša A., Orosz J. A., Welsh W. F., Bloemen S., Barclay T., 2012, ApJ, 143, 123
Montalto M. et al., 2021, A&A, 653, A98
Nascimbeni V. et al., 2022, A&A, 658, A31
Prša A. et al., 2011, ApJ, 141, 83
Rauer H. et al., 2014, Exp. Astron., 38, 249
Rauer H., Heras A. M., 2018, Space Missions for Exoplanet Science: PLATO. Springer Nature, Switzerland AG, p. 1309
Reid M. J., 1993, ARA&A, 31, 345
Ricker G. R. et al., 2014, J. Astron. Telesc. Instrum. Syst., 1, 014003
Rowden P., 2018, PhD thesis, The Open University, available at: http://oro.open.ac.uk/60434/
Sabotta S. et al., 2021, A&A, 653, A114
Slawson R. W. et al., 2011, ApJ, 142, 160
Southworth J., Bruntt H., Buzasi D. L., 2007, A&A, 467, 1215
Southworth J., Smalley B., Maxted P. F. L., Claret A., Etzel P. B., 2005, MNRAS, 363, 529
Southworth J., Zucker S., Maxted P. F. L., Smalley B., 2004, MNRAS, 355, 986
Van Cleve J. E., Caldwel D. A., 2016, in Haas M. R., Howell S. B., eds, Kepler Instrument Handbook (KSCI-19033-002). p. 1
Wade R. A., Rucinski S. M., 1985, A&AS, 60, 471
Willems B., Kolb U., 2002, MNRAS, 337, 1004
Willems B., Kolb U., 2004, A&A, 419, 1057
Willems B., Kolb U., Justham S., 2006, MNRAS, 367, 1103

This paper has been typeset from a TEX/LATEX file prepared by the author.